

ACE-Net: Fine-Level Face Alignment through Anchors and Contours Estimation

Jihua Huang

jihua.huang@sri.com

Amir Tamrakar

amir.tamrakar@sri.com

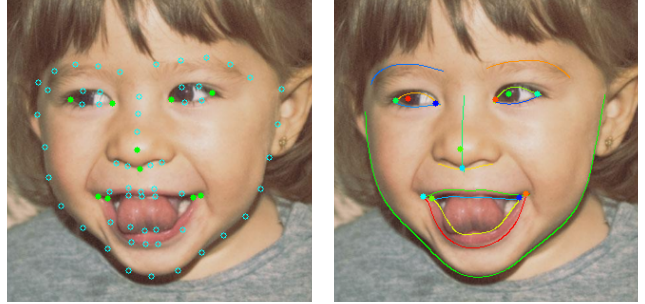
Center for Vision Technologies, SRI International

Abstract

We propose a novel facial **Anchors and Contours Estimation** framework, **ACE-Net**, for fine-level face alignment tasks. **ACE-Net** predicts facial anchors and contours that are richer than traditional facial landmarks and more accurate than facial boundaries. In addition, it does not suffer from the ambiguities and inconsistencies in facial-landmarks definitions. We introduce a weakly supervised loss enabling **ACE-Net** to learn from existing facial landmarks datasets without the need for extra annotations. Synthetic data is also used during training to bridge the density gap between landmarks annotation and true facial contours. We evaluate **ACE-Net** on commonly used face alignment datasets 300-W and HELEN, and show that **ACE-Net** achieves significantly higher fine-level face alignment accuracy than landmarks based models, without compromising its performance at the landmarks level. The proposed **ACE-Net** framework does not rely on any specific network architecture and thus can be applied on top of existing face alignment models for finer face alignment representation.

1. Introduction

Face alignment is the basis for various types of face analysis such as face reconstruction and visual speech recognition, where fine-level alignment is crucial. Most of the existing approaches use facial landmarks to perform face alignment. While the accuracy of facial landmarks detection has greatly improved over the past few years, there remain three major issues with facial landmarks representation: First, only a small subset of landmarks are well defined and can be localized fairly accurately, such as eye corners and those attached to local structures like pupils. We refer to these as *anchors*. The rest of the landmarks are just discrete points sampled along various facial contours. We call those *contour landmarks* as their positions are ambiguous along the contours (Fig. 1a). Second, facial landmarks are not dense enough to capture fine-level details of facial contours (Fig. 2). Third, facial landmarks definitions are sometimes different across existing datasets [22, 32, 43, 25]. To ad-



(a) Landmarks representation

(b) AC representation

Figure 1: Comparison between landmarks and AC representations. Anchors are marked with solid circles, contour landmarks with hollow circles, and contours with colored curves. Contour landmark positions are ambiguous since they can “slide” along their corresponding contours. There are also inconsistencies in the number of landmarks on each contour across different datasets. In contrast, AC is well defined and captures fine-level details.

dress the above issues, we propose facial **anchors and contours (AC)** as a fine-level representation for face alignment (Fig. 1b).

Facial boundary heatmaps is proposed by [43] to remove the ambiguities in the landmarks definition. Facial boundary heatmaps are a heatmaps representation of line-contours, which are obtained by connecting contour landmarks with line segments. While its application has shown consistent performance improvement in landmarks detection accuracy, there are two problems that prevent facial boundary heatmaps from being adopted as the final representation for face alignment: (1) no conversion exists from boundary heatmaps back to line-contours; and (2) their source, line-contours, are often not accurate enough at fine-level due to the insufficient density of facial landmarks (Fig. 2). Thus, facial boundary heatmaps have been used only as an internal intermediate representation to mitigate prediction errors caused by ill-defined landmarks.

To enable AC as the final output of face alignment models, we propose a framework, referred to as facial **Anchors and Contours Estimation Network (ACE-Net)**. **ACE-Net** consist of two modules: AC prediction and AC extraction. AC prediction module predicts AC heatmaps from input im-

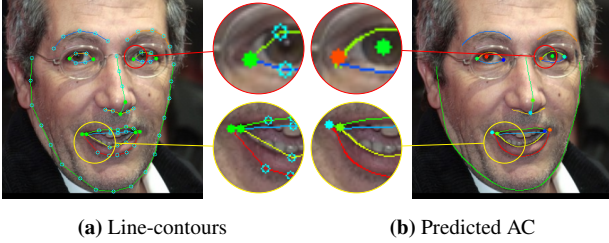


Figure 2: Comparison between line-contour representation and AC. (a) Line-contours generated from ground truth landmarks by connecting landmarks on the same contour. (b) AC predicted by ACE-Net. Despite being generated from ground truth landmarks, line contours are not accurate enough at fine level.

ages, and AC extraction converts AC heatmaps to raw AC representation with sub-pixel accuracy, allowing for subsequent quantitative analysis.

While being well defined and retaining finer details, facial contours are extremely time consuming to annotate precisely. To learn AC prediction models from existing facial landmarks datasets without re-annotation, we introduce a weakly supervised loss that enforces the predicted AC to pass through annotated facial landmarks. In addition, since the density of annotated landmarks is insufficient, we construct a synthetic training set rendered from 3D morphable face meshes where full AC annotations are easily accessible. We show that in spite of the domain gap, synthetic data improves fine-level accuracy in regions with no landmarks.

We evaluate our proposed method on two publicly available datasets: 300-W [32] and HELEN [25]. Both our qualitative and quantitative results show that at fine-level, ACE-Net outperforms landmarks based model by a large margin, especially in regions lacking training annotations. We also demonstrate the effectiveness of the proposed weakly supervised loss in leveraging the additional synthetic data and preventing models from overfitting to inaccurate line-contours.

In summary, our main contributions include:

- Proposing ACE-Net, the first facial alignment framework that predicts fine-level facial anchors and contours instead of facial landmarks.
- Devising a “contourness” loss to treat facial landmarks as weak supervision, allowing synthetic data with full supervision to complement the learning process.
- Introducing an AC extraction module that extracts anchors and contours from their heatmaps representation with subpixel accuracy.
- Defining an evaluation metric for the AC representation on facial landmarks datasets. We also show that compared to landmarks based or line-contours based models, ACE-Net achieves higher fine-level accuracy while maintaining similar landmarks-level accuracy.

2. Related Work

Classic face alignment approaches are mostly based on AAMs [6, 33, 35], ASMs [8, 9], CLMs [7, 34] or Cascaded Regression [13, 45]. Recent advances mainly focus on two major categories of deep learning based methods: coordinate regression and heatmap regression.

Coordinate regression Coordinate regression methods [36, 48, 39, 47, 40, 29] directly predict 2D coordinates of facial landmarks, usually adopting coarse-to-fine approaches with cascaded networks. [14] introduces wing loss which is less sensitive to outliers. Recently, [5, 17, 24] also measure prediction uncertainties besides their coordinates.

Heatmap regression Heatmap regression methods [42, 11, 10, 38] predict a heatmap for each facial landmark. Among all the network architectures, stacked hourglass (HG) network [30] is the most widely used among recent works [46, 3, 43]. Apart from commonly used L_1 or L_2 loss functions, [41] adapts wing loss from coordinate regression, and add different foreground and background weights to address the class imbalance in heatmaps. [19] introduces focal wing loss to adjust data sample weights. Currently, heatmap regression methods achieve higher accuracy compared to coordinate regression methods in general.

Facial boundary heatmaps To address the issue of ill-defined contour landmarks, [43] introduces facial boundary heatmaps which is the heatmaps representation of line-contours created from facial landmarks. Boundary heatmaps are also used in [41, 19] to improve landmarks prediction accuracy. Instead of modeling line-contours, ACE-Net predicts actual facial contours, retaining finer details in places where line-contours are inaccurate due to the insufficient density of facial landmarks annotations.

Face parsing Instead of predicting facial landmarks, face parsing methods [28, 50, 49, 27, 26] aim at segmenting faces into semantic face parts. Compared with facial landmarks models, face parsing models provide extra information such as skin masks and face part areas, but being segmentation models, their boundary predictions are less accurate and smooth compared to facial landmarks models.

Semi-supervised face alignment Under the assumption that large-scale accurately annotated facial landmarks datasets are difficult to obtain, [18] uses sequential multi-tasking and an unsupervised landmark transformation loss to reduce the need for large-scale data. [31] applies a GAN framework to leverage unlabelled data. [12] proposes a teacher-student interaction mechanism to iteratively improve generated pseudo labels for unlabelled data. In our paper, instead of dealing with inadequate amount of training samples, we focus on insufficient landmarks density and use synthetic data to help learn fine-level representations.

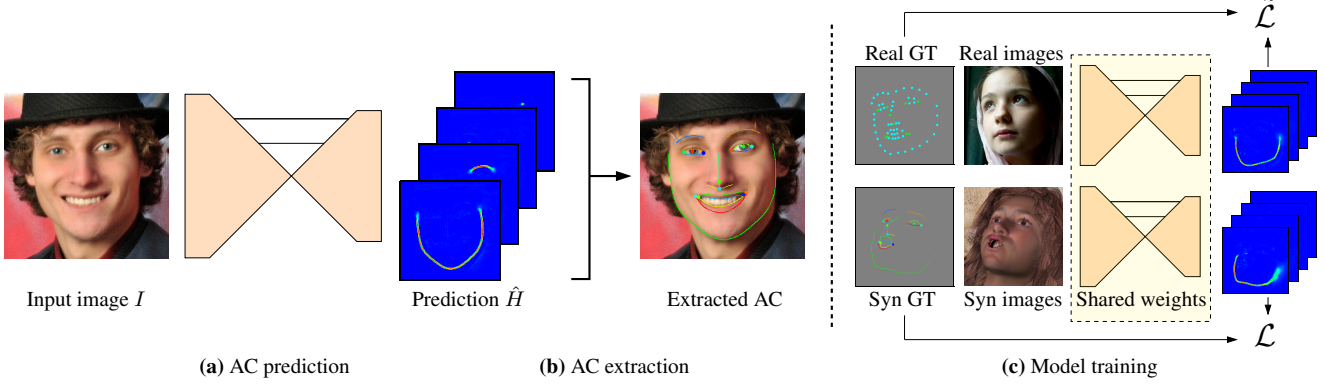


Figure 3: Overview of our ACE-Net framework. (a) AC prediction module that estimates the location of each anchor and contour with a heatmap. (b) AC extraction module that precisely localizes predicted anchors and contours from their heatmaps representations. (c) ACE-Net training framework. Fully supervised losses \mathcal{L} are applied to synthetic data where full AC annotations are available, while weakly supervised losses $\tilde{\mathcal{L}}$ are applied to real data where only landmarks annotations are available. Best viewed in color.

3. Methods

Fig. 3 shows an overview of our proposed ACE-Net framework. ACE-Net does not rely on any specific network architecture. We choose a Convolutional Pose Machine [42] based architecture due to its simplicity, but it can be replaced by any commonly used CNNs such as Stacked Hourglass [30]. At test time, with a cropped face image as the input, ACE-Net first predicts one heatmap per facial anchor and contour, and then performs AC extraction to locate each anchor and contour with sub-pixel accuracy. At training time, ACE-Net is trained with both synthetic and real images. The synthetic images are rendered from 3D face meshes and thus their ACs are automatically available, while the real images are annotated only with facial landmarks. We apply different losses to synthetic and real data due to the difference in their annotations. For real data we introduce weakly supervised loss functions, forcing the predicted contours to pass through annotated landmarks and stay close to the line-contours. For synthetic data we use the fully supervised loss as their AC annotations are available.

In this section we first introduce our AC representation, then we define our fully supervised and weakly supervised loss functions, and finally we describe our AC extraction module that enables explicit AC localization and evaluation.

3.1. AC Representation

For each face image I , landmarks representation selects landmarks $L = \{l_1, l_2, \dots, l_{N_L}\}$ as the output of face alignment models, where N_L is the total number of landmarks. For AC representation, we choose anchors $A = \{a_1, a_2, \dots, a_{N_A}\}$ and contours $C = \{c_1, c_2, \dots, c_{N_C}\}$ as the output where N_A and N_C are the total number of anchors and contours, respectively (Fig. 1b). Anchors are the subset of well-defined landmarks and each anchor a is

defined by its 2D coordinate (a_x, a_y) . Each contour c is defined by a set of line segments with two endpoints. To be accurate, contours with high curvatures often contain more line segments of very short length, even less than one pixel.

Anchor heatmap When predicting AC using CNNs, we represent each anchor and contour using one heatmap. Given an anchor $a = (a_x, a_y)$, we define its corresponding heatmap H_a as

$$H_a(p) = \max \left(0, 1 - 2 \frac{\|p - a\|^2}{\sigma^2} \right) \quad (1)$$

where $p = (x, y)$ is any pixel of H_a , and σ is the width of the peak. The above heatmaps representation has similar shape to commonly used Gaussian heatmaps representation. We pick this representation instead since it is consistent with our contour heatmap representation.

Contour heatmap Given a contour c defined by a set of line segments, we define its corresponding heatmap H_c as

$$H_c(p) = \max \left(0, 1 - 2 \frac{\text{dist}(p, c)^2}{\sigma^2} \right) \quad (2)$$

where $\text{dist}(p, c)$ is a function measuring the minimum distance from point p to any line segment in c .

3.2. Fully supervised loss

In fully supervised setting, for each image I , its anchors A and contours C are available. We generate the ground truth AC heatmaps H following Eq. 1 and Eq. 2, and define the fully supervised loss \mathcal{L} for predicted heatmaps \hat{H} as a weighted root mean square loss:

$$\mathcal{L}(H, \hat{H}) = \sqrt{\sum W(H, \hat{H}) \cdot \|H - \hat{H}\|^2} \quad (3)$$

where \cdot is element-wise multiplication, and W is a weighting emphasizing positive and hard negative examples:

$$W(H, \hat{H}) = 1 + \alpha \cdot \max(H, \|H - \hat{H}\|) \quad (4)$$

This weighting is necessary because most of the pixels in heatmaps are background pixels. Without W_h the learned model is easily trapped in the trivial local minimum $\hat{H} = 0$.

3.3. Weakly supervised loss

In weakly supervised setting, for each image I , only its landmarks L are available. For predicted anchor heatmaps \hat{H}_a we just apply the fully supervised loss \mathcal{L} in Eq. 3, since we have access to all ground truth anchors $A \subset L$.

On the other hand, while we can generate line-contours \tilde{C} from contour landmarks, often $\tilde{C} \neq C$ and thus applying fully supervised loss \mathcal{L} with \tilde{C} being the ground truth will result in loss in fine-level accuracy. Before we describe our weakly supervised contour loss $\tilde{\mathcal{L}}$, we first introduce a contourness score \mathcal{C} that evaluates whether there is a contour passing through a given pixel p on heatmap H . Assuming that contour is locally a straight line with orientation θ and width σ , we construct its heatmap template $T_{\sigma, \theta}$ based on Eq. 2:

$$T_{\sigma, \theta}(x, y) = \max\left(0, 1 - 2 \frac{(y \cos \theta - x \sin \theta)^2}{\sigma^2}\right) \quad (5)$$

Examples of $T_{\sigma, \theta}$ is shown in Fig. 4. If this contour passes through pixel p , then heatmap H cropped around p should match the template $T_{\sigma, \theta}$. Thus we define contourness score \mathcal{C} based on template matching error:

$$\begin{aligned} \mathcal{C}_\sigma(H, p) = & -\min_{\theta} \sum_{i=-2\sigma}^{2\sigma} \sum_{j=-2\sigma}^{2\sigma} G_\sigma(i, j) \cdot \\ & \|H_+(p_x + i, p_y + j) - T_{\sigma, \theta}(i, j)\|^2 \end{aligned} \quad (6)$$

where $H_+ = \max(0, H)$, and G_σ is a Gaussian weight:

$$G_\sigma(x, y) = e^{-\frac{x^2 + y^2}{\sigma^2}} \quad (7)$$

Since non-negative clipping is already applied to the signal H in Eq. 6, we will drop the clipping $\max(0, \cdot)$ for template $T_{\sigma, \theta}$ in Eq. 5 for the rest of the paper. We will also omit σ from function inputs and subscripts since it is a constant hyper-parameter.

To efficiently compute contourness \mathcal{C} for every pixel in heatmap H , Eq. 6 can be re-written as

$$\mathcal{C}(H) = 2 \max_{\theta} (H_+ \otimes (T_\theta \cdot G)) - H_+^2 \otimes G - T_\theta^2 \otimes G \quad (8)$$

where \otimes stands for convolution and \cdot stands for element-wise multiplication. Here the last term $T_\theta^2 \otimes G$ is a constant

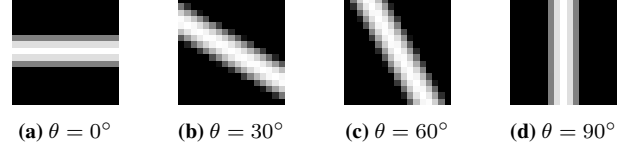


Figure 4: Contour template $T_{\sigma, \theta}$ with $\sigma = 4$ and size 17×17 .

and will be dropped. The convolution kernel $T_\theta \cdot G$ is a steerable filter [15] and therefore instead of exhaustively search across all orientations θ , $\max_{\theta} (H_+ \otimes (T_\theta \cdot G))$ can be efficiently computed by convolving H_+ with 3 convolution kernels:

$$\begin{aligned} G_{2a}(x, y) &= (1 - 2x^2/\sigma^2) \cdot G(x, y) \\ G_{2b}(x, y) &= -2xy/\sigma^2 \cdot G(x, y) \\ G_{2c}(x, y) &= (1 - 2y^2/\sigma^2) \cdot G(x, y) \end{aligned} \quad (9)$$

where $G(x, y)$ is the same as in Eq. 7. Thus, Eq. 8 can further be simplified as

$$\mathcal{C}(H) = R_a + R_c + \sqrt{(R_a - R_c)^2 + 4R_b^2} - H_+^2 \otimes G \quad (10)$$

where R_a, R_b, R_c are convolution responses of H_+ with filters G_{2a}, G_{2b}, G_{2c} , respectively.

With contourness score \mathcal{C} defined, let \hat{H} be a predicted contour heatmap representing a predicted contour \hat{c} , and \tilde{c} be its corresponding line-contour created from contour landmarks L_c , we build our weakly supervised loss to enforce the following three rules:

(1) The predicted contour \hat{c} must pass through all contour landmarks L_c :

$$\tilde{\mathcal{L}}_{\text{landmark}}(\hat{H}) = \sum_{l \in L_c} f(\mathcal{C}(\hat{H}, l)) \quad (11)$$

where $f(\cdot)$ is a mapping function that converts contourness from a score to a non-negative loss.

(2) The predicted contour \hat{c} must be close to line-contour \tilde{c} . In other words, for each pixel p on \tilde{c} , there must exist a pixel q on \hat{c} such that $q - p$ is the line-contour normal at p , and $\|p - q\| \leq D$ for some constant D :

$$\tilde{\mathcal{L}}_{\text{line}}(\hat{H}) = \sum_{p \text{ on } \tilde{c}} f\left(\max_{-D \leq d \leq D} \mathcal{C}(H, p + d \cdot \mathcal{N}_{\tilde{c}}(p))\right) \quad (12)$$

where $\mathcal{N}_{\tilde{c}}$ is the normal map of line-contour \tilde{c} and $\mathcal{N}_{\tilde{c}}(p)$ is the line-contour normal at p .

(3) Pixels far from line-contour \tilde{c} should have zero heat value:

$$\tilde{\mathcal{L}}_{\text{far}}(\hat{H}) = \sqrt{\sum M(\tilde{c}) \cdot |\hat{H}|^3} \quad (13)$$

where $M(\tilde{c})$ is a binary mask selecting pixels far from \tilde{c} :

$$M(\tilde{c}, p) = \begin{cases} 1, & \text{dist}(p, \tilde{c}) > D \\ 0, & \text{otherwise} \end{cases} \quad (14)$$

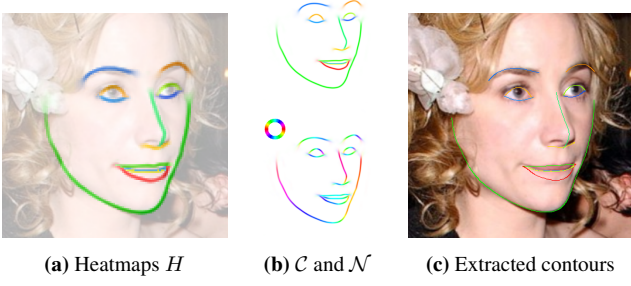


Figure 5: Contour extraction. (a) Contour heatmaps predicted by ACE-Net visualized on top of the input image. Due to space limitation we visualize heatmaps for all contours in one image with hue indicating contour ID and saturation indicating heat values. (b) Top: contourness map \mathcal{C} ; bottom: color coded normal map \mathcal{N} with normal orientation being hue and contourness being saturation. (c) Extracted contours.

Here $\text{dist}(\cdot, \cdot)$ is the same as in Eq. 2. We choose $|\hat{H}|^3 = |\hat{H}| \cdot \hat{H}^2$ as the loss as it is consistent with Eq. 3 (with ground truth $H = 0$).

Finally, we define our weakly supervised contour loss $\tilde{\mathcal{L}}$ as the sum of the three losses above:

$$\tilde{\mathcal{L}} = \tilde{\mathcal{L}}_{far} + \lambda_{landmark} \cdot \tilde{\mathcal{L}}_{landmark} + \lambda_{line} \cdot \tilde{\mathcal{L}}_{line} \quad (15)$$

where $\lambda_{landmark}$ and λ_{line} are constant weights.

3.4. AC Extraction

The AC Extraction module converts each predicted anchor heatmap to an anchor position $a = (a_x, a_y)$, and each contour heatmap to a list of line segments $c = \{s_i, i = 1, 2, \dots\}$.

Anchor We adopt the local center-of-mass method: given an anchor heatmap H , we find the pixel p^* with highest heat value, and compute anchor position a as

$$a = \sum_{p: \|p-p^*\| \leq \sigma} H(p) \cdot p \Big/ \sum_{p: \|p-p^*\| \leq \sigma} H(p) \quad (16)$$

Contour Given a contour heatmap H , we compute its contourness map $\mathcal{C}(H)$ according to Eq. 10, as well as its contour normal map using the following equation:

$$\begin{aligned} \mathcal{N}(H) &= \frac{\pi}{2} + \arg \max_{\theta} \mathcal{C}(H) \\ &= \frac{\arctan(2R_b, R_a - R_c)}{2} \end{aligned} \quad (17)$$

We perform non-maximum suppression on $\mathcal{C}(H)$ along directions specified by $\mathcal{N}(H)$, and extract foreground pixels P through hysteresis. We then connect all neighboring pixels in P into line segments $\{s_i, i = 1, 2, \dots\}$, forming the output contour c (Fig. 5).



Figure 6: Generated synthetic images and their AC annotations.

To extract contour c with sub-pixel level accuracy, say up to $1/k$ pixel, we shift the convolution kernels W , G_{2a} , G_{2b} and G_{2c} in Eq. 23 and Eq. 10 by multiples of $1/k$ along x and y directions respectively, and then merge the resulting contourness and normal maps. While such shifting results in k^2 times more convolution operations, they can be fully parallelized to minimize running time.

4. Synthetic Data Generation

Our synthetic training data is generated using a 3D morphable face model (3DMM) [1] created by [20]. We randomly select facial shape, expression and texture coefficients for the 3DMM and generate 55,000 3D face meshes with random accessories (hairs, glasses and headbands). Each mesh is rendered to a image with random lighting and head pose up to 60° yaw, 30° pitch and 30° roll. A random background image of non-human categories from Caltech-256 dataset [16] is added to each image during model training. We divide the images into a training set of 50,000 images and a test set of 5,000 images.

To obtain AC annotations for the synthetic data, we manually annotate the indices of all mesh vertices in the 3DMM corresponding to each facial anchor and contour. Since all generated meshes only differ in vertex coordinates and share the same vertex ordering, the manual annotation is only done once. With the vertex indices annotated we automatically generate the AC annotation for each image using the generated morph coefficients and head poses. Example synthetic images and their annotations are shown in Fig. 6.

5. Experiments

We evaluate our models on two publicly available datasets: 300-W and HELEN. On 300-W dataset, we measure the landmarks-level performance of our models, where both the training and test images are annotated with 68 landmarks. On HELEN dataset we measure the fine-level performance of our models pre-trained on 300-W training set. Since HELEN is annotated with 194 landmarks, significantly denser than 300-W, we can measure the fine-level accuracy of our models in places with no training annota-

tions. To the best of our knowledge, HELEN is the only currently available dataset with dense annotation for all face parts, especially for eyes and mouths.

5.1. Datasets

300-W [32] is the most widely used face alignment dataset where each image is annotated with 68 facial landmarks. It consists of a training set of 3148 images and two test sets: “Full” set contains 689 images in which 554 images belong to the common subset and the rest 135 images belong to the challenging subset, and “Private” set contains 600 images.

HELEN [25] is a densely annotated dataset with 194 facial landmarks. It contains 2000 training images and 330 test images. HELEN’s training and test images are subsets of 300-W’s training and test images, respectively, but HELEN’s annotation is much denser than 300-W and thus we use it to evaluate fine-level face alignment performance.

5.2. Evaluation Metrics

Normalized Mean Error (NME) is a standard metric to evaluate landmarks based face alignment models:

$$\text{NME}(L, \hat{L})(\%) = \frac{100}{d} \cdot \frac{1}{N_L} \sum_{i=1}^{N_L} \|l_i - \hat{l}_i\|_2 \quad (18)$$

where \hat{L} is the predicted landmarks and L is the ground truth landmarks. d is the normalization factor. For all experiments in this paper, we use inter-ocular distance (distance between the two outer eye corners) as the normalization factor in order to be consistent with existing works.

To evaluate AC based face alignment models with a similar metric, we divide L into anchor landmarks $L^A = A$ and contour landmarks L^C such that $l_i^A = a_i$ and L_i^C is the set of landmarks on contour c_i . Each and every contour landmark corresponds to one contour. In this case, the NME for predicted anchors \hat{A} and contours \hat{C} is defined as:

$$\text{NME}(L, \hat{A}, \hat{C})(\%) = \frac{100}{d} \cdot \frac{1}{N_L} \cdot \left(\sum_{i=1}^{N_A} \|l_i^A - \hat{a}_i\|_2 + \sum_{i=1}^{N_L - N_A} \text{dist}(l_i^C, \hat{c}_i) \right) \quad (19)$$

where $\text{dist}(\cdot, \cdot)$ is the point-to-contour distance same as in Eq. 2.

Area Under the Curve (AUC) is another widely used metric. It measures the area under the cumulative error distribution (CED) curve with the error being NME. We cut off the error at 10% to be consistent with existing works.

Failure Rate (FR) measures the proportion of predictions whose error is larger than a threshold. We set the threshold to 10% to be consistent with existing works.

5.3. Implementation Details

During training, we obtain face bounding boxes by padding the tight boxes from ground truth landmarks by 25%, 25%, 33%, 17% on left, right, top and bottom sides respectively, and then convert them into square boxes by keeping the longest edge length. Our training data augmentation includes random translation up to 25%, rotation up to 30°, horizontal flipping with 50% chance, gamma correction with $\gamma \in (2^{-0.75}, 2^{0.75})$ and Gaussian noise. We set anchor and contour width $\sigma = 2$, and contourness pooling radius $D = 6$ for our weakly supervised losses in Eq. 12 and Eq. 13.

Our network has an input size of 256×256 (grayscale) and an output size of $128 \times 128 \times (N_A + N_C)$ where N_A and N_C are the number of anchors and contours, respectively. Details of our network architecture are described in our supplementary materials due to space limitations. We train our models from scratch using Adam optimizer [21] with an initial learning rate of 2.5×10^{-4} , fuzz factor at 10^{-8} and learning rate decay at 10^{-6} . All our models are trained with three 8GB GeForce GTX 1080 GPUs.

During testing, for 300-W split 1, we use the provided face bounding boxes to replace the tight bounding boxes from landmarks, then pad and square the boxes same as in the training phase. For 300-W split 2 and HELEN we still use the tight boxes since no bounding boxes are provided. For AC extraction we use $\sigma = 3$ and sub-pixel accuracy $k = 3$. We choose a larger σ than in training because the predicted heatmaps tend to be more “spread out” than the ground truth.

5.4. Landmarks-level evaluation on 300-W

We evaluate the landmarks-level performance of ACE-Net on 300-W dataset. We also create two baseline models: Lmk and Lmk-line. **Lmk** is an ordinary facial landmark heatmaps regression model. It predicts facial landmarks using the same network architecture as ACE-Net, and is trained with fully supervised loss (\mathcal{L} in Eq. 3). **Lmk-line** adds a post-process to Lmk which converts its predicted landmarks to anchors and line-contours. This model is a proxy enabling fair comparisons between Lmk and AC based models under the same evaluation metrics.

Table 1 compares ACE-Net, Lmk and Lmk-line with state-of-the-art methods. Our baseline model Lmk achieves near SOTA performance in spite of its simple architecture and training loss. By comparing the performance difference between Lmk and Lmk-line which share the same underline model, we observe that a large portion of the prediction error (47.8% in Full set and 43.8% in Private set) is contributed by the error along contours, where the ground truth is not clearly defined. We made similar observations on WFLW dataset [43] where this proportion is 39.8%. Due to space limitations we describe detailed results on WFLW

Model	Full		Private	
	NME	AUC	NME	AUC
PCD-CNN [23]	4.44	-	-	-
SAN [11]	3.98	-	-	-
LAB [43]	3.49	-	-	58.85
DU-Net [37]	3.35	-	-	-
AWing [41]	3.07	-	3.56	64.40
3FabRec [2]	3.82	-	-	54.61
LUVLi [24]	3.23	-	-	-
PropNet [19]	2.93	-	-	-
Lmk	3.93	64.04	4.93	57.01
Lmk-line	2.05	80.38	2.77	74.59
ACE-Net	2.12	81.81	3.24	75.83

Table 1: NME and AUC on 300-W testsets

dataset in our supplementary materials. This observation justifies the need for face alignment representations such as AC, and their corresponding evaluation metrics, that do not suffer from such ambiguities in the ground truth.

At landmarks-level, ACE-Net shows similar performance to the baseline model Lmk-line with slightly higher NME (0.07 on Full set and 0.47 on Private set) but higher AUC (1.43 on Full set and 1.24 on Private set). This result matches our expectation since the additional synthetic data used in ACE-Net training aim to improve its accuracy mostly in places without landmarks annotation.

5.5. Fine-level evaluation on HELEN

To evaluate the fine-level performance, we train our models on 300-W training set and evaluate them on HELEN test set where the annotated landmarks are significantly denser than in 300-W. We exclude eyebrow landmarks from evaluation because their physical definitions are different between 300-W (eyebrow center-lines) and HELEN (eyebrow boundaries).

To analyze the impact of the generated synthetic data and our proposed weakly supervised losses $\hat{\mathcal{L}}$, we create two models for ablation study: **Line** and **Line***. They only differ from ACE-Net in the training data and losses:

Model	Training data	Loss
Line	Real	\mathcal{L}
Line*	Real + Syn	\mathcal{L}
ACE-Net	Real + Syn	\mathcal{L} for Syn + $\hat{\mathcal{L}}$ for Real

Here “Real” stands for 300-W training set and “Syn” stands for the generated synthetic data. Among these models, Line is the equivalent of facial boundary heatmaps models.

Table 2 lists NME of our models on HELEN. To the best of our knowledge, our work is the first to tackle fine-level face alignment, and there are no other SOTA methods to compared with on this dataset. We also show the CED curves as well as AUC and FR results in Fig. 7.

Model	Overall	Eyes	Nose	Mouth	Chin
Lmk-line	2.25	1.64	2.14	2.81	2.12
Line	1.63	1.27	1.17	1.43	2.34
Line*	1.62	1.20	1.16	1.40	2.42
ACE-Net	1.37	0.97	1.18	1.37	1.80

Table 2: NME on HELEN testset

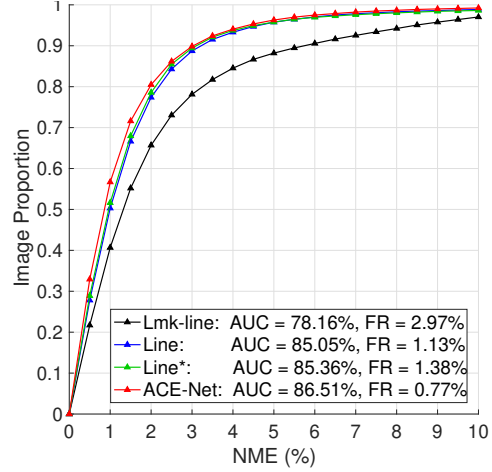


Figure 7: CED curve on HELEN testset

Table 2 and Fig. 7 show that at fine-level, ACE-Net (NME = 1.37 and AUC = 86.51%) achieves significantly better accuracy than Lmk-line (NME = 2.25 and AUC = 78.16%) in all face parts. ACE-Net also outperforms the facial boundary based model, Line, especially towards the low-error end. For example, ACE-Net correctly fits 56.7% of the landmarks with no more than 1 NME whereas Line only fits 50.3%.

We also observe that without applying the proposed weakly supervised loss to the real training data, adding synthetic data alone does not bring any notable improvement. Line* has extremely close performance to Line: its overall NME is merely 0.01 lower than Line and its AUC is only 0.31% higher. Due to the large domain gap between the synthetic and the real data, Line* easily overfits to the inaccurate line-contours in the real data, and thus does not benefit from the more accurate synthetic annotations. However, in ACE-Net, our proposed weakly supervised loss prevents the model from learning from inaccurate portions of the real line-contours and therefore synthetic data brings significant improvement over to Line.

5.6. Qualitative results

Fig. 8 provides a qualitative comparison between Lmk-line, Line and ACE-Net models. It illustrates that landmarks and their corresponding line-contours predicted by Lmk-line are not accurate representations of true facial contours because the number of landmarks are limited. Facial bound-

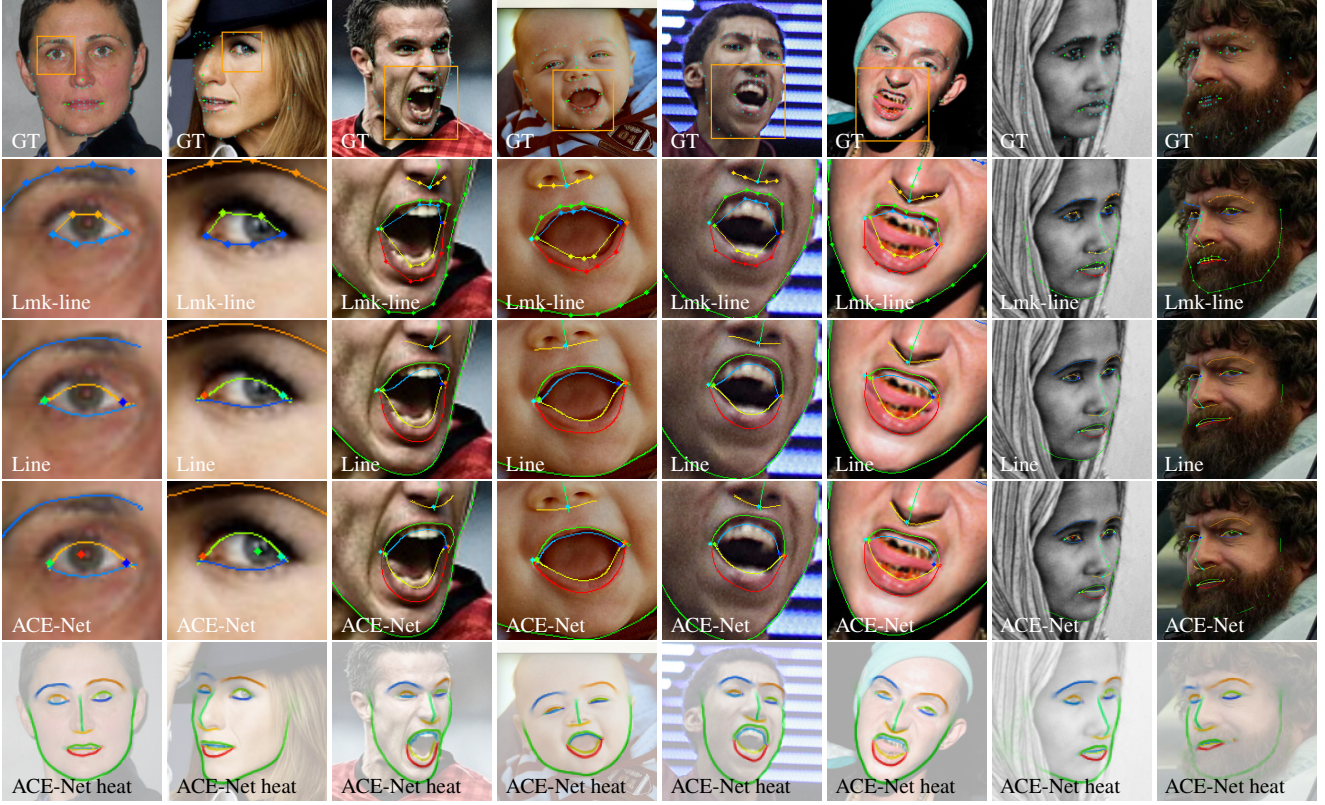


Figure 8: Qualitative results on 300-W testset. Each of the five rows shows (1) ground truth landmarks; (2) Lmk-line results; (3) Line results; (4) ACE-Net results; and (5) AC heatmaps predicted by ACE-Net. Due to space limitations, for some results we only show a small patch cropped using the bounding boxes visualized in the first row. Compared to other models, ACE-Net best captures fine-level details, especially at places with no landmarks. The last two columns show examples of failure cases due to occlusion: there is large ambiguity around chin contours and thus the predicted contour heat values are too weak and spread out for the AC extraction module to pick up.

aries predicted by Line appear more accurate, but they are really a smoothed version of Lmk-line’s line-contours and do not always follow local image cues, exhibiting similar error patterns as Lmk-line. In contrast, ACE-Net predicts facial contours whose shapes are more consistent with true facial contours, especially in places lacking training annotations such as inner lips.

The last two columns in Fig. 8 show the most common failure case of AC based models. When there is significant ambiguity in the position of a contour, for example, when there are severe occlusion, our AC extraction may fail to extract any contour if the predicted contour heatmaps do not contain any strong sharp ridges. However, in such cases fine-level alignment is usually out of the question anyway.

6. Conclusion

In this paper, we present ACE-Net, the first face alignment framework that learns fine-level facial anchors and contours prediction models. Compared to landmarks or line-contours based models, ACE-Net captures fine-level

details of face structures with higher accuracy, especially in regions lacking annotations at training time. Our experiments show that such accuracy is achieved by our novel weakly supervised losses that prevent the model from over-fitting to inaccurate landmarks based line-contours, and instead learn from accurately annotated synthetic data. ACE-Net demonstrates the potential of synthetic data as a complement to sparsely labelled real data: when treating the sparsely labelled real data as weak supervision, synthetic data are able to bridge the density gap and improve fine-level prediction accuracy of the learned models.

7. Supplementary

7.1. Derivation of Equations

In this section we provide the derivation of Contourness $\mathcal{C}(H)$ (Eq. 10 in the main paper) and Normal map $\mathcal{N}(H)$ (Eq. 17 in the main paper). We start from Eq. 8 in the main paper, where $\mathcal{C}(H)$ is defined in a convolutional form:

$$\mathcal{C}(H) = 2 \max_{\theta} (H_{+} \otimes (T_{\theta} \cdot G)) - H_{+}^2 \otimes G - T_{\theta}^2 \otimes G \quad (8)$$

here $H_+ = \max(0, H)$, T_θ and G are defined in the main paper as

$$T_\theta(x, y) = 1 - 2 \frac{(y \cos \theta - x \sin \theta)^2}{\sigma^2} \quad (5)$$

$$G(x, y) = e^{-\frac{x^2+y^2}{\sigma^2}} \quad (7)$$

We drop the non-negative clipping for the template T_θ since we already apply such clipping to the signal H (by turning it to H_+).

Since G is invariant to θ , the last term $T_\theta^2 \otimes G$ is a constant number and is dropped. Thus we compute $\mathcal{C}(H)$ as

$$\mathcal{C}(H) = 2 \max_\theta (H_+ \otimes (T_\theta \cdot G)) - H_+^2 \otimes G \quad (20)$$

Here $T_\theta \cdot G$ is the same as the steerable filter G_2 in Table III from [15]. According to [15], with G_{2a} , G_{2b} and G_{2c} being

$$\begin{aligned} G_{2a}(x, y) &= \left(1 - \frac{2x^2}{\sigma^2}\right) e^{-\frac{x^2+y^2}{\sigma^2}} \\ G_{2b}(x, y) &= -\frac{2xy}{\sigma^2} e^{-\frac{x^2+y^2}{\sigma^2}} \\ G_{2c}(x, y) &= \left(1 - \frac{2y^2}{\sigma^2}\right) e^{-\frac{x^2+y^2}{\sigma^2}} \end{aligned} \quad (21)$$

we can compute $H_+ \otimes (T_\theta \cdot G)$ as

$$\begin{aligned} H_+ \otimes (T_\theta \cdot G) &= (H_+ \otimes G_{2a}) \cdot \sin^2 \theta \\ &\quad - (H_+ \otimes G_{2b}) \cdot 2 \cos \theta \sin \theta \\ &\quad + (H_+ \otimes G_{2c}) \cdot \cos^2 \theta \end{aligned} \quad (22)$$

(Note that our filters and coefficients definition here are slightly different from Table III in [15], because θ in [15] is defined as the normal instead of the contour orientation.) Let R_a , R_b , R_c be the convolution responses:

$$\begin{aligned} R_a &= H_+ \otimes G_{2a} \\ R_b &= H_+ \otimes G_{2b} \\ R_c &= H_+ \otimes G_{2c} \end{aligned} \quad (23)$$

then Eq. 22 becomes

$$\begin{aligned} H_+ \otimes (T_\theta \cdot G) &= R_a \sin^2 \theta - R_b \cdot 2 \cos \theta \sin \theta + R_c \cos^2 \theta \\ &= R_a \frac{1 - \cos 2\theta}{2} - R_b \sin 2\theta + R_c \frac{1 + \cos 2\theta}{2} \\ &= \frac{R_c + R_a}{2} + \frac{R_c - R_a}{2} \cos 2\theta - R_b \sin 2\theta \\ &= \frac{R_c + R_a}{2} + \\ &\quad \cos(2\theta - \phi) \sqrt{\left(\frac{R_c - R_a}{2}\right)^2 + R_b^2} \end{aligned} \quad (24)$$

Thus we have

$$\max_\theta (H_+ \otimes (T_\theta \cdot G)) = \frac{R_c + R_a}{2} + \sqrt{\left(\frac{R_c - R_a}{2}\right)^2 + R_b^2} \quad (25)$$

and

$$\arg \max_\theta (H_+ \otimes (T_\theta \cdot G)) = \frac{\phi}{2} = \frac{\arctan(-2R_b, R_c - R_a)}{2} \quad (26)$$

By plugging Eq. 25 back to Eq. 20, we get Eq. 10 in the main paper:

$$\mathcal{C}(H) = R_a + R_c + \sqrt{(R_a - R_c)^2 + 4R_b^2} - H_+^2 \otimes G \quad (10)$$

And from Eq. 26 we get Eq. 17 in the main paper:

$$\begin{aligned} \mathcal{N}(H) &= \frac{\pi}{2} + \arg \max_\theta \mathcal{C}(H) \\ &= \frac{\pi + \arctan(-2R_b, R_c - R_a)}{2} \\ &= \frac{\arctan(2R_b, R_a - R_c)}{2} \end{aligned} \quad (17)$$

7.2. Example Network Architecture

Fig. 9 fully illustrates the architecture of our example ACE-Net model used for our experiments. We predict $N_A = 12$ anchors and $N_C = 13$ contours per image (i.e., $K = 25$ heatmaps per image). The names of anchors and contours are listed in Table 3. Our example architecture is picked due to its simplicity (inference takes around 17ms per image on a 8GB GeForce GTX 1080 GPU). Since our model has intermediate outputs, we apply losses to intermediate outputs as well for better intermediate supervision. Because the intermediate outputs have very low resolution equal to 1/8 of the input, we just treat line-contours as ground truth and apply fully supervised loss. This intermediate loss is not required, especially when a network architecture without intermediate outputs (such as Stacked Hourglass) is chosen instead. ACE-Net does not rely on any specific network architecture.

7.3. Additional Experiments

7.3.1 Landmarks-level Evaluation on WFLW

In addition to the 300-W dataset, we also evaluate the landmarks-level performance of our models on the WFLW [43] dataset. WFLW dataset has 7500 training images and 2500 test images, each annotated with 98 landmarks.

Table 4 shows the landmarks-level accuracy of our models as well as the SOTA methods. By comparing the performance difference between Lmk and Lmk-line which share the same underline model, we observe that 39.42% of the prediction error is contributed by the error along contours,

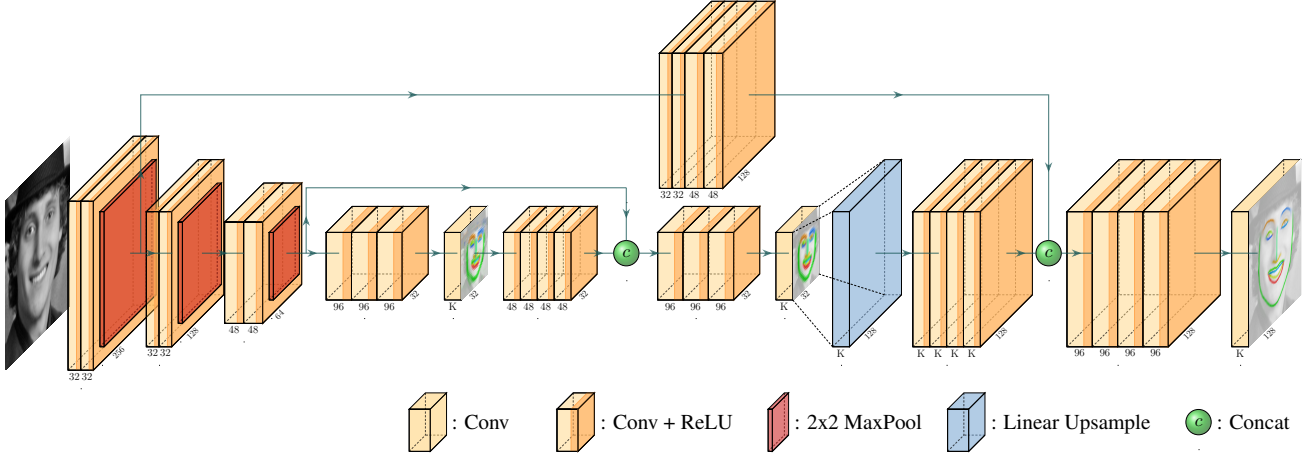


Figure 9: Network architecture of our example ACE-Net model with all filter sizes and layer sizes annotated. Zoom in for a clearer view. K is the number of heatmaps for each image. Our example architecture takes grayscale images as input and outputs 3 sets of AC heatmaps (the output layers are visualized with heatmaps overlay). The first two sets of heatmaps are only used for intermediate supervision at training time, and are ignored at test time.

Anchors	Contours
right eye inner corner	right eyebrow center-line
right eye outer corner	left eyebrow center-line
left eye inner corner	right eye upper lid
left eye outer corner	right eye lower lid
right iris center	left eye upper lid
left iris center	left eye lower lid
nose tip	nose ridge
nose bottom center	nose bottom boundary
mouth right outer corner	mouth upper lip outer
mouth left outer corner	mouth lower lip outer
mouth right inner corner	mouth upper lip inner
mouth left inner corner	mouth lower lip inner
	chin boundary

Table 3: List of facial anchors and contours. The definitions of anchors and contours are illustrated by figures in the main paper.

Model	NME	AUC	FR
ESR [4]	11.13	27.74	35.24
SDM [45]	10.29	30.02	29.40
CFSS [51]	9.07	36.59	20.56
DVLN [44]	6.08	45.51	10.84
LAB [43]	5.27	53.23	7.56
AWing [41]	4.36	57.19	2.84
3FabRec [2]	5.62	48.4	8.28
LUVLi [24]	4.37	57.7	3.12
PropNet [19]	4.05	61.58	2.96
Lmk	6.90	55.03	14.56
Lmk-line	4.18	68.96	7.22
ACE-Net	5.82	72.09	8.97

Table 4: Landmarks-level eval on WFLW testset

where the ground truth is not clearly defined. We also observe that at the landmarks level, ACE achieves similar performance to the baseline model Lmk-line with slightly higher NME (1.64) but higher AUC (3.13), which is consistent with our results on 300-W dataset.

7.3.2 Robustness against Sparse Training Annotation

To further illustrate the robustness of ACE-Net against insufficient training annotation density, we train another ACE-Net model on 300-W training set only with 36 annotated landmarks (Fig. 10). We refer to this model as **ACE-Net^{sparse}**. All its hyper-parameters, loss functions and the use of synthetic training data is the same as the original ACE-Net. We evaluated its fine-level performance on HELEN testset and compare it with the other models from the main paper.

Table 5 and Fig. 11 show the performance comparison on HELEN testset. Although ACE-Net^{sparse} is trained with only 36 landmarks, its performance (NME = 1.46 and AUC = 85.57%) is close to ACE-Net (NME = 1.37 and AUC = 86.51%) which is trained with all 68 landmarks. We also observe that ACE-Net^{sparse} outperforms Lmk-line, Line and Line*, despite them all being trained with 68 landmarks. In particular, ACE-Net^{sparse} outperforms Lmk-line by a large margin (with 0.79 NME and 7.41% AUC difference). This comparison show the ability of ACE-Net to leverage the synthetic data to make up for the insufficient annotation density in the real data.

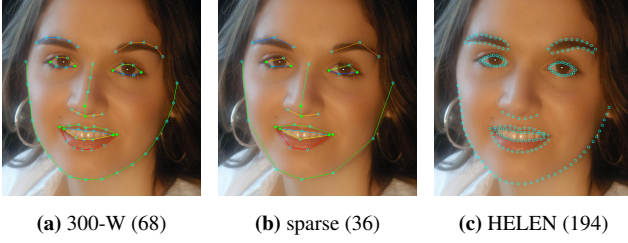


Figure 10: Comparison of landmarks annotations. (a) 68-landmark annotation in 300-W. (b) 36-landmark sparse annotation used to train ACE-Net^{sparse}. (c) 194-landmark annotation in HELEN which we evaluate with.

Model	Overall	Eyes	Nose	Mouth	Chin
Lmk-line	2.25	1.64	2.14	2.81	2.12
Line	1.63	1.27	1.17	1.43	2.34
Line*	1.62	1.20	1.16	1.40	2.42
ACE-Net	1.37	0.97	1.18	1.37	1.80
ACE-Net ^{sparse}	1.46	0.99	1.20	1.38	2.04

Table 5: NME on HELEN testset

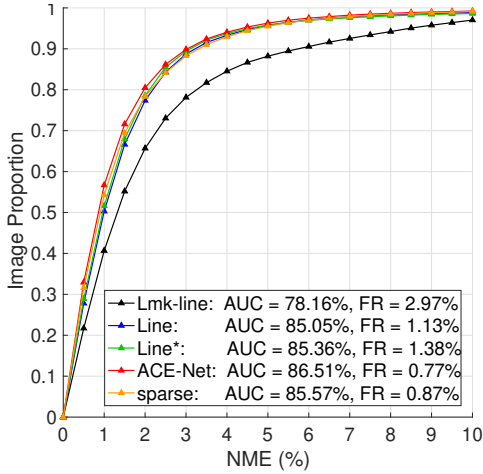


Figure 11: CED curve on HELEN testset. ACE-Net^{sparse} is labelled as “sparse” in the figure due to space limitation.

References

- [1] Volker Blanz and Thomas Vetter. A morphable model for the synthesis of 3d faces. In *Proceedings of the 26th annual conference on Computer graphics and interactive techniques*, pages 187–194, 1999. 5
- [2] Bjorn Browatzki and Christian Wallraven. 3fabrec: Fast few-shot face alignment by reconstruction. In *Proceedings of the IEEE/CVF Conference on Computer Vision and Pattern Recognition*, pages 6110–6120, 2020. 7, 10
- [3] Adrian Bulat and Georgios Tzimiropoulos. How far are we from solving the 2d & 3d face alignment problem?(and a dataset of 230,000 3d facial landmarks). In *Proceedings of the IEEE International Conference on Computer Vision*, pages 1021–1030, 2017. 2
- [4] Xudong Cao, Yichen Wei, Fang Wen, and Jian Sun. Face alignment by explicit shape regression. *International Journal of Computer Vision*, 107(2):177–190, 2014. 10
- [5] Lisha Chen, Hui Su, and Qiang Ji. Face alignment with kernel density deep neural network. In *Proceedings of the IEEE International Conference on Computer Vision*, pages 6992–7002, 2019. 2
- [6] Timothy F. Cootes, Gareth J. Edwards, and Christopher J. Taylor. Active appearance models. *IEEE Transactions on pattern analysis and machine intelligence*, 23(6):681–685, 2001. 2
- [7] Tim F Cootes, Mircea C Ionita, Claudia Lindner, and Patrick Sauer. Robust and accurate shape model fitting using random forest regression voting. In *European Conference on Computer Vision*, pages 278–291. Springer, 2012. 2
- [8] Timothy F Cootes and Christopher J Taylor. Active shape models—‘smart snakes’. In *BMVC92*, pages 266–275. Springer, 1992. 2
- [9] Timothy F Cootes, Christopher J Taylor, David H Cooper, and Jim Graham. Active shape models-their training and application. *Computer vision and image understanding*, 61(1):38–59, 1995. 2
- [10] Jiankang Deng, George Trigeorgis, Yuxiang Zhou, and Stefanos Zafeiriou. Joint multi-view face alignment in the wild. *IEEE Transactions on Image Processing*, 28(7):3636–3648, 2019. 2
- [11] Xuanyi Dong, Yan Yan, Wanli Ouyang, and Yi Yang. Style aggregated network for facial landmark detection. In *Proceedings of the IEEE Conference on Computer Vision and Pattern Recognition*, pages 379–388, 2018. 2, 7
- [12] Xuanyi Dong and Yi Yang. Teacher supervises students how to learn from partially labeled images for facial landmark detection. In *Proceedings of the IEEE International Conference on Computer Vision*, pages 783–792, 2019. 2
- [13] Zhen-Hua Feng, Guosheng Hu, Josef Kittler, William Christmas, and Xiao-Jun Wu. Cascaded collaborative regression for robust facial landmark detection trained using a mixture of synthetic and real images with dynamic weighting. *IEEE Transactions on Image Processing*, 24(11):3425–3440, 2015. 2
- [14] Zhen-Hua Feng, Josef Kittler, Muhammad Awais, Patrik Huber, and Xiao-Jun Wu. Wing loss for robust facial landmark localisation with convolutional neural networks. In *Proceedings of the IEEE Conference on Computer Vision and Pattern Recognition*, pages 2235–2245, 2018. 2
- [15] William T Freeman, Edward H Adelson, et al. The design and use of steerable filters. *IEEE Transactions on Pattern analysis and machine intelligence*, 13(9):891–906, 1991. 4, 9
- [16] Gregory Griffin, Alex Holub, and Pietro Perona. Caltech-256 object category dataset. 2007. 5
- [17] Nitesh B Gundavarapu, Divyansh Srivastava, Rahul Mitra, Abhishek Sharma, and Arjun Jain. Structured aleatoric uncertainty in human pose estimation. In *CVPR Workshops*, volume 2, 2019. 2
- [18] Sina Honari, Pavlo Molchanov, Stephen Tyree, Pascal Vincent, Christopher Pal, and Jan Kautz. Improving landmark

- localization with semi-supervised learning. In *Proceedings of the IEEE Conference on Computer Vision and Pattern Recognition*, pages 1546–1555, 2018. 2
- [19] Xiehe Huang, Weihong Deng, Haifeng Shen, Xiubao Zhang, and Jieping Ye. Propagationnet: Propagate points to curve to learn structure information. In *Proceedings of the IEEE/CVF Conference on Computer Vision and Pattern Recognition*, pages 7265–7274, 2020. 2, 7, 10
- [20] Singular Inversions Inc. Facegen modeller pro (3.22). 5
- [21] Diederik P Kingma and Jimmy Ba. Adam: A method for stochastic optimization. *arXiv preprint arXiv:1412.6980*, 2014. 6
- [22] Martin Koestinger, Paul Wohlhart, Peter M Roth, and Horst Bischof. Annotated facial landmarks in the wild: A large-scale, real-world database for facial landmark localization. In *2011 IEEE international conference on computer vision workshops (ICCV workshops)*, pages 2144–2151. IEEE, 2011. 1
- [23] Amit Kumar and Rama Chellappa. Disentangling 3d pose in a dendritic cnn for unconstrained 2d face alignment. In *Proceedings of the IEEE Conference on Computer Vision and Pattern Recognition*, pages 430–439, 2018. 7
- [24] Abhinav Kumar, Tim K Marks, Wenxuan Mou, Ye Wang, Michael Jones, Anoop Cherian, Toshiaki Koike-Akino, Xiaoming Liu, and Chen Feng. Luvli face alignment: Estimating landmarks’ location, uncertainty, and visibility likelihood. In *Proceedings of the IEEE/CVF Conference on Computer Vision and Pattern Recognition*, pages 8236–8246, 2020. 2, 7, 10
- [25] Vuong Le, Jonathan Brandt, Zhe Lin, Lubomir Bourdev, and Thomas S Huang. Interactive facial feature localization. In *European conference on computer vision*, pages 679–692. Springer, 2012. 1, 2, 6
- [26] Jinpeng Lin, Hao Yang, Dong Chen, Ming Zeng, Fang Wen, and Lu Yuan. Face parsing with roi tanh-warping. In *Proceedings of the IEEE Conference on Computer Vision and Pattern Recognition*, pages 5654–5663, 2019. 2
- [27] Sifei Liu, Jianping Shi, Ji Liang, and Ming-Hsuan Yang. Face parsing via recurrent propagation. *arXiv preprint arXiv:1708.01936*, 2017. 2
- [28] Sifei Liu, Jimei Yang, Chang Huang, and Ming-Hsuan Yang. Multi-objective convolutional learning for face labeling. In *Proceedings of the IEEE Conference on Computer Vision and Pattern Recognition*, pages 3451–3459, 2015. 2
- [29] Jiangjing Lv, Xiaohu Shao, Junliang Xing, Cheng Cheng, and Xi Zhou. A deep regression architecture with two-stage re-initialization for high performance facial landmark detection. In *Proceedings of the IEEE conference on computer vision and pattern recognition*, pages 3317–3326, 2017. 2
- [30] Alejandro Newell, Kaiyu Yang, and Jia Deng. Stacked hourglass networks for human pose estimation. In *European conference on computer vision*, pages 483–499. Springer, 2016. 2, 3
- [31] Joseph P Robinson, Yuncheng Li, Ning Zhang, Yun Fu, and Sergey Tulyakov. Laplace landmark localization. In *Proceedings of the IEEE International Conference on Computer Vision*, pages 10103–10112, 2019. 2
- [32] Christos Sagonas, Georgios Tzimiropoulos, Stefanos Zafeiriou, and Maja Pantic. 300 faces in-the-wild challenge: The first facial landmark localization challenge. In *2013 IEEE International Conference on Computer Vision Workshops*, pages 397–403. IEEE, 2013. 1, 2, 6
- [33] Jason Saragih and Roland Goecke. A nonlinear discriminative approach to aam fitting. In *2007 IEEE 11th International Conference on Computer Vision*, pages 1–8. IEEE, 2007. 2
- [34] Jason M Saragih, Simon Lucey, and Jeffrey F Cohn. Deformable model fitting by regularized landmark mean-shift. *International journal of computer vision*, 91(2):200–215, 2011. 2
- [35] Patrick Sauer, Timothy F Cootes, and Christopher J Taylor. Accurate regression procedures for active appearance models. In *BMVC*, pages 1–11, 2011. 2
- [36] Yi Sun, Xiaogang Wang, and Xiaoou Tang. Deep convolutional network cascade for facial point detection. In *Proceedings of the IEEE conference on computer vision and pattern recognition*, pages 3476–3483, 2013. 2
- [37] Zhiqiang Tang, Xi Peng, Shijie Geng, Lingfei Wu, Shaoting Zhang, and Dimitris Metaxas. Quantized densely connected u-nets for efficient landmark localization. In *Proceedings of the European Conference on Computer Vision (ECCV)*, pages 339–354, 2018. 7
- [38] Zhiqiang Tang, Xi Peng, Kang Li, and Dimitris N Metaxas. Towards efficient u-nets: A coupled and quantized approach. *IEEE Transactions on Pattern Analysis and Machine Intelligence*, 2019. 2
- [39] Alexander Toshev and Christian Szegedy. Deeppose: Human pose estimation via deep neural networks. In *Proceedings of the IEEE conference on computer vision and pattern recognition*, pages 1653–1660, 2014. 2
- [40] George Trigeorgis, Patrick Snape, Mihalis A Nicolaou, Epameinondas Antonakos, and Stefanos Zafeiriou. Mnemonic descent method: A recurrent process applied for end-to-end face alignment. In *Proceedings of the IEEE Conference on Computer Vision and Pattern Recognition*, pages 4177–4187, 2016. 2
- [41] Xinyao Wang, Liefeng Bo, and Li Fuxin. Adaptive wing loss for robust face alignment via heatmap regression. In *Proceedings of the IEEE International Conference on Computer Vision*, pages 6971–6981, 2019. 2, 7, 10
- [42] Shih-En Wei, Varun Ramakrishna, Takeo Kanade, and Yaser Sheikh. Convolutional pose machines. In *Proceedings of the IEEE conference on Computer Vision and Pattern Recognition*, pages 4724–4732, 2016. 2, 3
- [43] Wayne Wu, Chen Qian, Shuo Yang, Quan Wang, Yici Cai, and Qiang Zhou. Look at boundary: A boundary-aware face alignment algorithm. In *Proceedings of the IEEE conference on computer vision and pattern recognition*, pages 2129–2138, 2018. 1, 2, 6, 7, 9, 10
- [44] Wenyan Wu and Shuo Yang. Leveraging intra and inter-dataset variations for robust face alignment. In *Proceedings of the IEEE conference on computer vision and pattern recognition workshops*, pages 150–159, 2017. 10
- [45] Xuehan Xiong and Fernando De la Torre. Supervised descent method and its applications to face alignment. In *Proceed-*

- ings of the *IEEE conference on computer vision and pattern recognition*, pages 532–539, 2013. 2, 10
- [46] Jing Yang, Qingshan Liu, and Kaihua Zhang. Stacked hourglass network for robust facial landmark localisation. In *Proceedings of the IEEE Conference on Computer Vision and Pattern Recognition Workshops*, pages 79–87, 2017. 2
 - [47] Jie Zhang, Shiguang Shan, Meina Kan, and Xilin Chen. Coarse-to-fine auto-encoder networks (cfan) for real-time face alignment. In *European conference on computer vision*, pages 1–16. Springer, 2014. 2
 - [48] Erjin Zhou, Haoqiang Fan, Zhimin Cao, Yuning Jiang, and Qi Yin. Extensive facial landmark localization with coarse-to-fine convolutional network cascade. In *Proceedings of the IEEE international conference on computer vision workshops*, pages 386–391, 2013. 2
 - [49] Lei Zhou, Zhi Liu, and Xiangjian He. Face parsing via a fully-convolutional continuous crf neural network. *arXiv preprint arXiv:1708.03736*, 2017. 2
 - [50] Yisu Zhou, Xiaolin Hu, and Bo Zhang. Interlinked convolutional neural networks for face parsing. In *International symposium on neural networks*, pages 222–231. Springer, 2015. 2
 - [51] Shizhan Zhu, Cheng Li, Chen Change Loy, and Xiaoou Tang. Face alignment by coarse-to-fine shape searching. In *Proceedings of the IEEE conference on computer vision and pattern recognition*, pages 4998–5006, 2015. 10